Hindawi

Research Article

Modeling and Simulation of the Aerodynamic Noise of High-Speed Train's Pantograph

R. E. Shaltout [ID],[1,2] **N. M. Aljameel,**[1] **and A. F. AbdelGawad** [ID][1]

[1]*Mechanical Power Engineering Department, Faculty of Engineering, Zagazig University, Zagazig 44519, Egypt*
[2]*Faculty of Engineering and Materials Science, German University in Cairo, Cairo 11835, Egypt*

Correspondence should be addressed to R. E. Shaltout; ramy.shaltout@guc.edu.eg

This article aims to investigate the aerodynamic noise of the pantograph of the high-speed trains in different operating conditions. CFD technique was used to assess the acoustic noise of the pantograph components. Three-dimensional computational simulations were performed using FLUENT software. Comprehensive analyses of the acoustic pressure and the air velocity distributions were accomplished for the detailed full-scale pantograph components. Good agreement was found between the obtained results and the reported results in the literature. Vortex shedding was the main source of noise at the pantograph panhead and knee. A modified model for the pantograph was introduced to reduce the aerodynamic noise of the pantograph's panhead. A different design profile for the collector was presented as a possible solution for the reduction of both the aerodynamic noise and the reduction of the fluctuating forces at the panhead-catenary interaction, which affects the quality of the power transmitted to the high-speed train. The cylindrical cross-section of the panhead bars was replaced with different cross-sections. It was noticed that at a speed of 250 km/hr, the use of an elliptic cross-section has resulted in an almost 23.1% reduction in the acoustic sound pressure for the pantograph.

1. Introduction

Due to the large expansion in the transportation systems around the world, the use of high-speed trains (HST) has been significantly developed in the last 50 years. Important measures have been taken to improve the environmental sustainability of high-speed rail systems. One of the most important measures is noise mitigation, which improves the impact of the HST on the environment [1]. Thus, it is crucial for all HST operators and infrastructure managers to determine the main sources of noise.

These sources of noise in high-speed systems include the following: the aerodynamic noise, the turbulent boundary layer (TBL) noise, the rolling noise, the equipment noise, car interspacing noise, and traction noise [2–4]. However, for the high-speed rail systems, especially above 250 km/h, the dominant sources of noise are the wheel/rail interaction (rolling) noise and the aerodynamic noise [2, 5].

The influence of the aerodynamic noise is notable for velocities above 220 km/h. For velocities above 350 km/h, it was noticed that the noise from train aerodynamics becomes considerable compared with the rolling noise [2]. At a train speed of 370 km/h, the aerodynamic noise contribution becomes higher than the rolling contact noise contribution in the global pass-by noise [1, 2]. The aerodynamic noise mainly comes from the aeroacoustics sources, namely, the pantograph and the TBL [6]. When dealing with aeroacoustics in HST, two phenomena should be considered: the first is the generated noise by the airflow around train structure elements, which might include the cavity and vortex shedding noises; the second is the turbulent flow noise [1]. Various studies were reported in the literature on the aerodynamic performance of high-speed trains at different operating conditions, including windbreaks and crosswinds [7–13]. However, most of the research work in the literature addressing the aerodynamics of the

pantograph systems only focuses on the vibration of the catenary caused by the impact of the pantograph. The influence of the environmental perturbation was seldom considered [5].

Various studies have been reported to assess the aerodynamic performance of the pantograph of high-speed trains [14–16]. In fact, the noise of aeroacoustics from pantographs during high-speed operation has become one of the major sources of noise of any train, which must be decreased to meet standards of environment that limit road noise. Therefore, there is a strong demand to reduce the aerodynamic noise of pantographs in order to reduce noise in the rail environment. Hence, to achieve this goal, continuous efforts have led to the development of low-noise pantographs.

Poissons [5] reported that the pantograph noise was the main source of the aerodynamic noise for Shinkansen E2-1000 running at a speed of 360 km/h. An experimental investigation was carried out by Nagakura [17] to determine the sources of noise in Shinkansen trains. Wind tunnel tests for a model of a 1/5-scale train were compared to field noise measurements with an acoustic mirror. It was found that the front pantograph noise was the most dominant source of the noise. Lee et al. [18] investigated experimentally the aerodynamic characteristics of the KTX-II high-speed train pantograph system in a wind tunnel. They demonstrated an optimized pantograph panhead to enhance the aerodynamic drag and lift forces on the pantograph.

Wind tunnel experiments have been carried out to assess the pantograph aerodynamic performance [19–22]. Lolgen et al. [19] carried out wind tunnel tests for a full-scale pantograph model at air speeds up to 400 km/h. They noticed that a strong noise, caused by vortex shedding, was detected from the strips presenting the contact of the pantograph with the catenary line. Lauterbach et al. [21] performed an aeroacoustics wind tunnel test to measure the weighted sound pressure level (SPL) time history for a 1/25-scale of the ICE3 high-speed train model. They noted that, at frequencies above 5000 Hz for a 1/25-scale mock-up, the dominant noise is the pantograph noise. Recently, Noh [23] investigated experimentally the aeroacoustics noise generated by major parts of a full-scale pantograph at different air speeds using wind tunnel tests. It was found that the pantograph panhead and the knee are the main sources of noise generated by the pantograph.

Due to the complexity of the pantograph system, field measurements were difficult to define the aerodynamic noise that comes from the pantograph components. Therefore, computational investigations have been carried out using CFD models to simulate the level of noise and determine the sound pressure spectrum of the high-speed pantograph system [24–27]. Using the results of the computational simulations, new designs and modifications can be performed on the pantograph to enhance noise and sound exposure levels in a high-speed train environment [14,27–30]. An empirical aerodynamic noise model was presented by Zhang et al. [3]. Based on their model, the aerodynamic noise can be estimated by subtracting the rolling noise calculated by the indirect roughness method

(IRM) from the total measured pass-by noise. Xiao-Ming et al. [31] computationally investigated the aeroacoustics behavior of the Faiveley CX-PG high-speed pantograph. They found that the vortex structure produced in the flow field around the pantograph is the main dominating noise source, especially at the pantograph insulator, upper and bottom frames, and the lower arm. They concluded that the aerodynamic noise can be reduced by the variation of the vortices shedding positions.

It is important to carefully investigate the impact of changing the geometry of the panhead components. A trade-off always exists between the stability of the pantograph and the reduction in the generated aerodynamic noise. Suzuki et al. [32] proposed a new design technique for the geometry of the pantograph panhead. The new design proposed by Suzuki et al. takes into consideration the balance between the lift force and the generated aerodynamic noise from the panhead. In the literature, most of the researchers investigated the aerodynamic performance and the noise generated from the whole pantograph. But, a comprehensive study of the noise generated from each of the pantograph components should be performed. A semiempirical model was proposed by Iglesias et al. [27] to predict the aerodynamic noise generated from each component of the pantograph of the high-speed train. Each component was approximated to be cylindrical with a specified cross-section. Square, rectangular, circular, and elliptical sections were investigated. The noise generated by the vortex shedding from each pantograph bar was then independently calculated.

A 1/3-scale model of the pantograph panhead collectors was experimentally studied in a wind tunnel by Takaishi and Ikeda [33]. They used L-shape angles spoilers as obstacles to the flow. They were able to determine the aerodynamic noise generated by the panhead collector and the noise generated by the obstacles themselves. Ikeda et al. [30] proposed a shape-optimization for the pantograph panhead, in addition to covering the articulate frame and surface with a porous material. They performed a modification to the pantograph panhead by introducing 20 holes with a diameter of 6 mm and 20 mm long, penetrating the panhead to reduce the intense Aeolian tone generation from the panhead collector. They noticed that although the optimized shape of the panhead could considerably reduce the aerodynamic noise, the generated aerodynamic noise by the optimized panhead attached to the articulated pantograph frame could not be reduced especially in the high-frequency range.

Based on the above literature survey, we conclude that to decrease the noise level of a pantograph, it is necessary to comprehend the mechanism of noise generation for a pantograph. However, it is problematic to estimate this mechanism by analogy. Thus, the present work aims to investigate the aerodynamic performance of the SSS87 pantograph and computationally assess the acoustic noise emissions of the pantograph at different operating conditions. The obtained results were validated using the computational and experimental results reported in the literature. Further modifications on the pantograph panhead were investigated, and the computational simulation of these modifications is presented.

2. Description of the Pantograph Model

All modern high-speed train networks around the world are electrified. The pantograph is the component that provides the rolling stock with the power transmitted through the catenary line. The dynamic interaction between the catenary and the pantograph has utmost importance in maintaining a stable power transmission to the rolling stocks. Various studies have been carried out to simulate and investigate the characteristics of the pantograph-catenary interaction [34]. Most of the current designs of the pantograph systems are scissors-type except Shinkansen 500 series, which has a telescopic pantograph system [35]. In general, any existing pantograph topologies should provide three main functions: panhead lifting to maintain contact with the catenary wire; dealing with the displacements caused by the passage of middle arms; managing the high-amplitude excitations caused at low frequencies during operation [36]. The pantograph consists of many complex subcomponents, which affects the aerodynamics of the pantograph.

The SSS87 pantograph model in this article is the high-speed pantograph [38,39]. Figure 1 depicts a 3D model of the articulated frame of the pantograph. The technical data of the SSS87 articulated pantograph is defined in Table 1. The panhead represents the critical part influencing the aerodynamic performance in the high-speed pantograph system. The SSS87 articulated pantograph consists of a four-bar mechanism that guides the pantograoh in approximately verticla manner and is composed of a lower arm, upper arm, and coupling rod, in addition to the base frame. The pantograph lifting and lowering can be produced at different operating speeds according to the operator's specifications. For producing a contact between the panhead and the catenary line, an air spring bellow is used for lifting the pantograph. The pantograph is lowered through its own weight after the air spring bellow by discharging the bellow from the compressed air.

3. Computational Model Description

The proposed computational domain in this work was defined in FLUENT software package version 18.2. The complete computational domain for a full pantograph model is represented in Figure 2. It has a cylindrical form with a diameter of $2L = 3$ m and a length of $4L = 6$ m. $L = 1.5$ m, which represents the characteristic length shown in Figure 1. As the SSS87 pantograph is symmetrical, a symmetry plan was introduced to consider only half the domain surrounding the pantograph in order to reduce the computational run-time, as shown in Figure 3(a). The inlet condition to the domain was defined as the value of the air velocity without turbulent fluctuations. "Pressure outlet" condition was defined at the exit as seen in Figure 3(b). At the boundary, the pressure value was specified to "uniform pressure." As the flow is considered as noncompressible subsonic flow, the pressure outlet boundary condition requires the definition of the value of the specified static pressure at the outlet boundary.

3.1. Simulation Criteria.

To calculate the flow around the pantograph model, CFD analysis is usually used. However, computational aeroacoustics (CAA) is used to numerically analyze the level of noise generated by the pantograph components [5]. The analysis used a 3D flow field with pressure-based transient solver to consider the vortex shedding. A realizable k-ε turbulence model was used in the simulations. The inlet and exit boundary conditions to the flow domain were set to be uniform velocity and uniform pressure gradient, respectively. External surface and object surface were defined as cell zone conditions. Wall function was used to define the boundary condition at the walls.

Usually, the value of the time step and the number of time steps are selected based on the aeroacoustic requirements. For the present simulations, the second-order implicit scheme was used with a time step equal to 2.5×10^{-4} s. The number of time steps was set to 400. The computational simulations were carried out in ANSYS software version 18.2. More information about all the flow governing equations for the developed model can be provided in the user manual [40].

3.2. Mesh Sensitivity Analysis.

Achieving a good accuracy of the simulation results depends mainly on the computational grid size. The element size in the grid should not exceed 1/5 of the flow wavelength considered. Mesh refinement was applied at the wall boundaries and the pantograph frame. Initially, an element size of 0.04 m was considered to validate the obtained results with the experimental and computational results in the literature [38, 39].

Further refinement procedure was assumed to adopt the accuracy of the computational results. Thus, a mesh-element size of 0.00004 m was used for simulation purposes in the present work. Figure 4 represents the variation of the maximum static pressure at the pantograph's panhead with grid size. The number of elements used in the full computational model of the pantograph was 22 million elements. The number of mesh elements of the symmetric model that gives the accurate and best result is selected to be 1.34 million elements corresponding to the point highlighted in Figure 4. As can be seen in Figure 4, there is no change in the value of the static pressure with a further increase in the number of grid elements above 1.34 million. In order to capture the viscous effects associated with the developed boundary layer around the pantograph elements, mesh refinement was carried out around the pantograph and the wall boundaries as shown in Figure 5.

3.3. Acoustic Model.

The literature survey of the aeroacoustics performance of the high-speed pantographs revealed that the near-field and far-field sound pressure level of the pantograph can be determined by the application of the Acoustic Perturbation Equation (APE) and Ffowcs Williams and Hawkings (FW-H) approaches, respectively. Based on unsteady flow simulations, the APE [41] approach is applicable for the calculations of the near-

1) Support insulator

2) Basic frame

3) Bellows

4) Lower arm

5) Upper arm

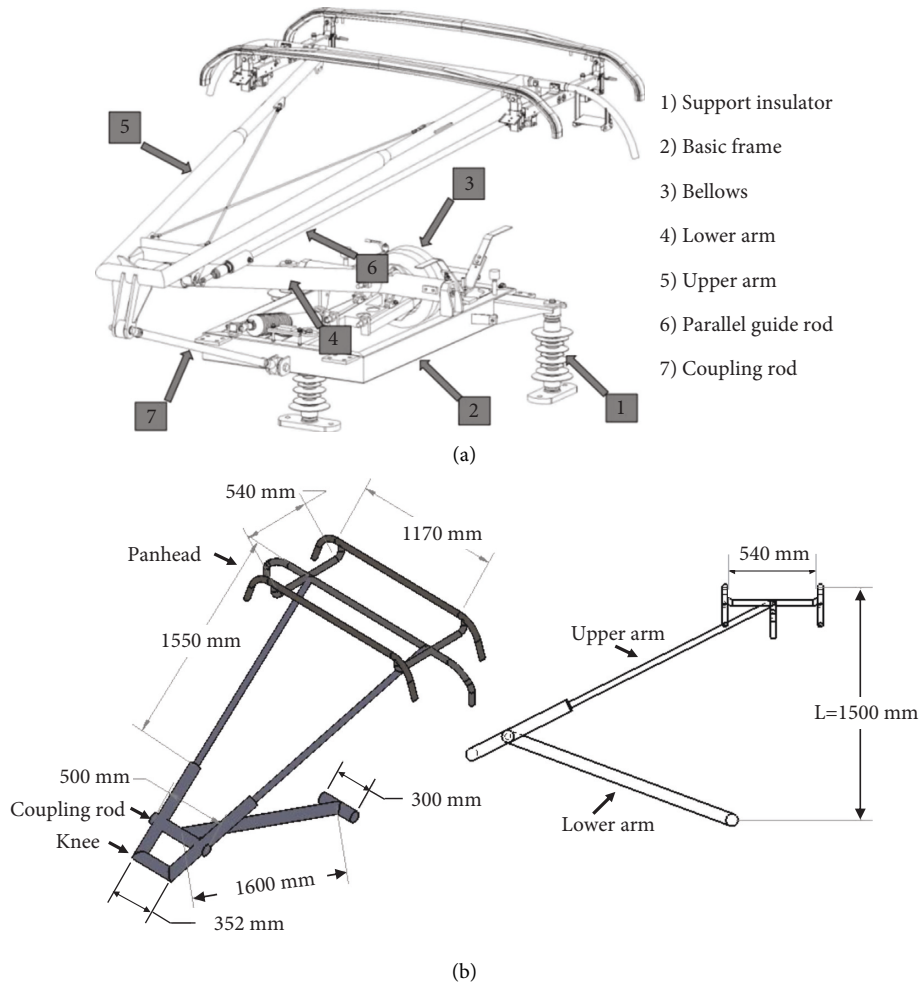6) Parallel guide rod

7) Coupling rod

(a)

(b)

Figure 1: (a) Actual description of SSS87 pantograph [37]; (b) schematic description of SSS87 articulated pantograph model.

Table 1: Technical data of SSS87 articulated pantograph [37].

Part description	Value
Standard overall height in the lowered state	600 mm
Maximum height above the lowered state	2400 mm
Minimum height above the lowered state	300 mm
Lifting height	>2500 mm
Nominal insulation	25 kV
Nominal current with carbon	1000 A
Nominal current with metal impregnated carbon	2200 A
Contact force	40–150 N
Total weight including insulator	135 kg

field sound pressure calculations as it presents an explicit description of the acoustic level by solving the unsteady fluid flow simultaneously with the sound pressure in the time domain [42]. Many approaches have been used to investigate the aerodynamic noise characteristics for the pantograph of high-speed trains. However, Ffowcs Williams-Hawkings (FW-H) equation [43] was widely used to simulate the flow field and the noise radiated from the far-field of the pantograph components [31, 44–46]. In the present investigation, the aeroacoustics noise generated from the pantograph is then predicted by using the FW-H approach. As the computational simulations of the generated noise from the pantograph of high-speed trains are extensive, this article only focuses on the characteristics of far-field noise generated by the SSS87 articulated pantograph components.

The FW-H equation is derived by rearranging the exact Navier–Stokes and continuity equations. Integral techniques can be used for the wave propagation simulation to predict the noise signal from the far-field based on the inputs from near-filed. Although the solution of the FW-H equation evolves both surface and volume integrals, the solution is usually approximated by only the surface integral [47]. In the simulations of aeroacoustics of high-speed trains, the FW-H method is often applied by integrating the surface coinciding with the solid bodies, such as the case in the pantograph. However, the method is also functional in the case where the surface is permeable and off the body. In the present investigation, all pantograph components are treated as impermeable surfaces for sound sources in the FW-H approach. The sound is radiated from the sound source surfaces to the far-field point receivers. The FW-H equation can be expressed in the differential form as follows:
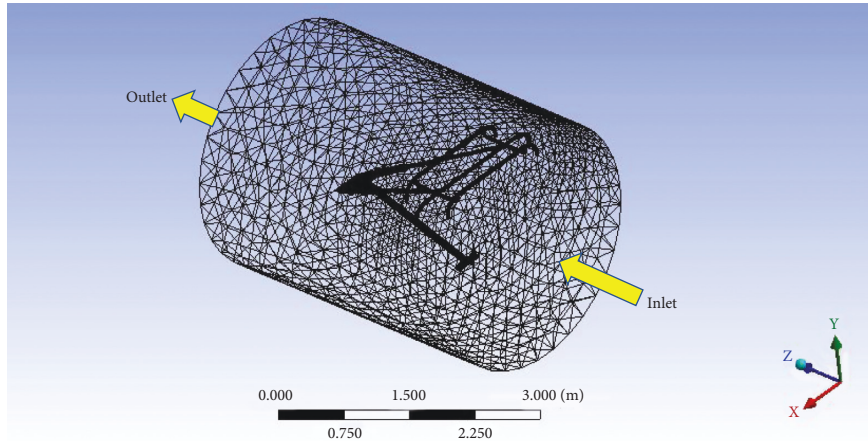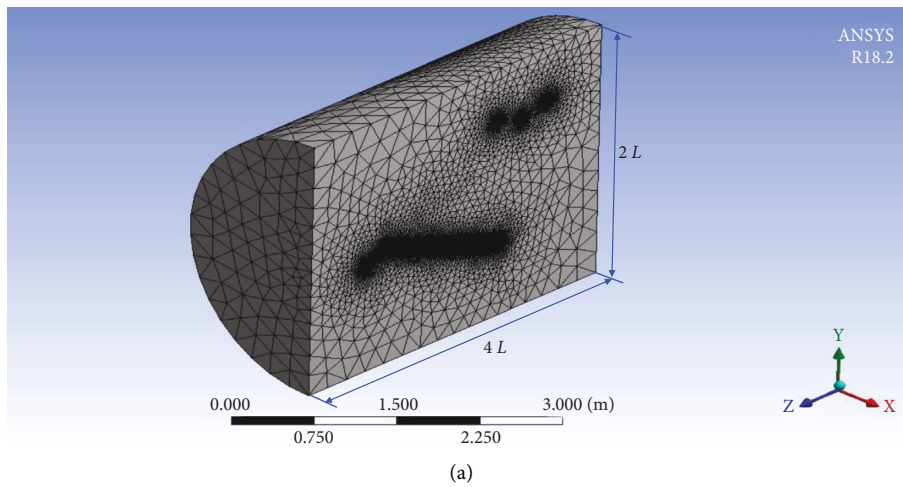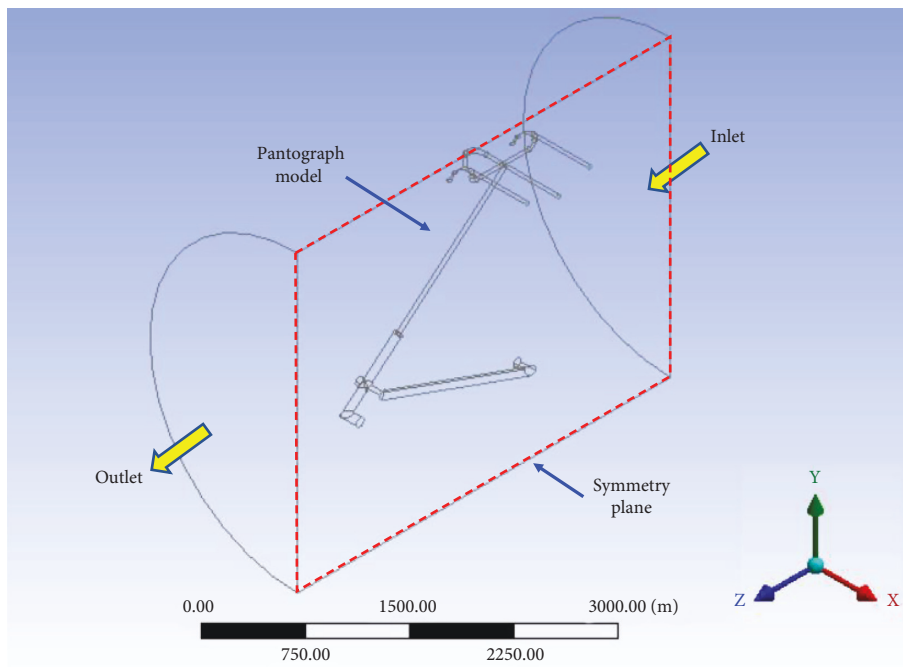
Figure 2: Proposed computational domain for a complete model of the pantograph.

(a)

(b)

Figure 3: Proposed computational domain for a symmetric model of the pantograph.
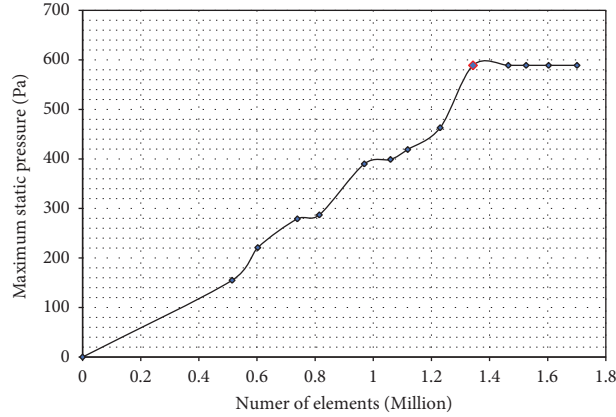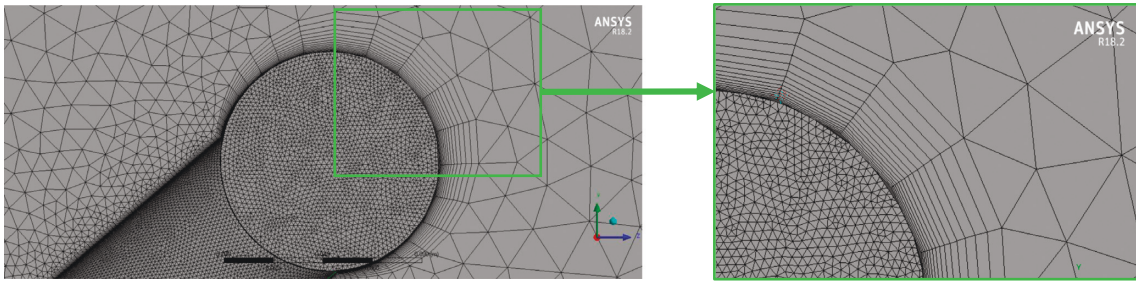
FIGURE 4: Mesh sensitivity test.

FIGURE 5: Mesh refinement around the pantograph elements.

$$\left(\frac{\partial^2}{\partial t^2} - C_o^2 \frac{\partial^2}{\partial x_i \partial x_j}\right)(H(f)'\rho) = \frac{\partial^2}{\partial x_i \partial x_j}\left(T_{ij}H(f)\right)$$
$$\qquad\qquad - \frac{\partial}{\partial x_i}\left(F_i \delta(f)\right) + \frac{\partial}{\partial t}\left(Q\delta(f)\right), \tag{1}$$

where

$$T_{ij} = \rho u_i v_j + P_{ij} - C_o^2 \prime \rho \delta_{ij}, \tag{2}$$

$$F_i = \left(P_{ij} - \rho u_i \left(u_i - v_j\right)\right)\frac{\partial f}{\partial x_i}, \tag{3}$$

$$Q = \left(\rho_o v_j + \rho\left(u_i - v_j\right)\right)\frac{\partial f}{\partial x_i}. \tag{4}$$

The quadrupole sound source term in the right-hand side of equation (1) is defined by the Lighthill stress tensor T_{ij}. The dipole term is defined as the vector F_i, while the monopole contribution is denoted by Q that represents unsteady mass addition which can be ignored as the pantograph objects are considered rigid bodies. The simulations were carried out at different train speeds of 300, 320, and 340 km/hr, which corresponds to associated Mach numbers of 0.242, 0.242, 0.258, and 0.274, respectively. The ratio between the quadrupole to the dipole terms was found to be proportional to the square value of the associated Mach number [48]. The generated noise intensity of the quadrupole contribution is too small compared to the dipole source contribution as the pantograph is still running at low subsonic speeds [45]. The free stream conditions were

denoted with the subscript "o," while the perturbation quantities are distinguished by the prime. The surfaces outside the desired solution region are defined by the function $f = 0$ and $|\nabla f| = 1$. The Heaviside function $H(f)$ is defined as follows:

$$\left\{\begin{array}{l} H(f) = 1 \ \text{ for } f > 0 \\ H(f) = 0 \ \text{ for } f < 0 \end{array}\right\}. \tag{5}$$

The Dirac delta $\delta(f)$ presents the derivative of Heaviside function $H\prime(f)$, while Kronecker delta in equation (2) is defined as follows:

$$\left\{\begin{array}{l} \delta_{ij} = 1 \ \text{ for } i = j \\ \delta_{ij} = 0 \ \text{ for } i \neq j \end{array}\right\}. \tag{6}$$

P defines the pressure and the density is defined by ρ. u_i presents the fluid velocity at the surface normal direction and v_j is the moving body's velocity at the surface in normal direction. The Green function [49] is usually used for solving equation (1) in the time domain. Another alternative approach can be used for solving the FW-H equation in the frequency domain; for more details, see [47, 50].

4. Aerodynamic Flow Characteristics of the Pantograph

Generally, the computation fluid dynamics (CFD) have been widely used for the study of the aerodynamic performance of high-speed trains. The traditional CFD approach begins with defining the partial differential Navier–Stokes equations,

which statistically describe fluid flow behavior in the continuum approximation [7]. Recently, the lattice Boltzmann method (LBM) has received considerable attention as a modern computational fluid dynamics in microscopic space models [51]. Various studies have been reported in the literature for the study of the aeroacoustics and aerodynamics of high-speed trains using LBM [11, 12]. This is due to the fact that LBM has some advantages compared to the other traditional approach as Navier–Stokes equations, including handling complex geometric setups, parallelization computations, and the simplicity of computational algorithms. The numerical solver used in the present research is the commercial CFD code FLUENT, which is part of the ANSYS 18.2 software. Pressure-based transient solver is used for all simulations due to the turbulent nature of the slipstream around the pantograph components. As the flow is considered a noncompressible subsonic flow, the Navier–Stokes equations were still applicable to control volume around the pantograph, as described in Figure 2. Hence, the resulting equations for a Newtonian fluid with constant density and viscosity can be described as follows:

$$\rho g_x - \frac{\partial p}{\partial x} + \mu \left(\frac{\partial^2 u}{\partial x^2} + \frac{\partial^2 u}{\partial y^2} + \frac{\partial^2 u}{\partial z^2} \right) = \rho \frac{du}{dt}, \tag{7}$$

$$\rho g_y - \frac{\partial p}{\partial x} + \mu \left(\frac{\partial^2 v}{\partial x^2} + \frac{\partial^2 v}{\partial y^2} + \frac{\partial^2 v}{\partial z^2} \right) = \rho \frac{dv}{dt}, \tag{8}$$

$$\rho g_z - \frac{\partial p}{\partial z} + \mu \left(\frac{\partial^2 w}{\partial x^2} + \frac{\partial^2 w}{\partial y^2} + \frac{\partial^2 w}{\partial z^2} \right) = \rho \frac{dw}{dt}. \tag{9}$$

The described Navier–Stokes equations relate density (ρ), viscosity (μ), and pressure (p) of a Newtonian fluid, where u, v, and w represent the velocity vector components in x, y, and z, respectively. The fluctuations in the velocity and pressure for incompressible turbulent flow present additional complications for the Navier–Stokes equations, which can be presented as follows:

$$\frac{\partial \overline{u}}{\partial t} + \overline{u} \frac{\partial \overline{u}}{\partial x} + \overline{v} \frac{\partial \overline{u}}{\partial y} + \overline{w} \frac{\partial \overline{u}}{\partial z} = -\frac{1}{\rho} \frac{\partial \overline{p}}{\partial x} + \frac{\mu}{\rho} \left(\frac{\partial^2 \overline{u}}{\partial x^2} + \frac{\partial^2 \overline{u}}{\partial y^2} + \frac{\partial^2 \overline{u}}{\partial z^2} \right)$$
$$- \frac{\partial}{\partial x} \overline{u}^2 - \frac{\partial}{\partial y} \overline{uv} - \frac{\partial}{\partial z} \overline{uw}. \tag{10}$$

Unsteady Reynolds-Averaged Navier–Stokes (URANS) model was adopted in the current simulations. The governing equations include the conservation of mass, momentum, and energy. The main idea behind using URANS rather than other approaches is that it was necessary to simulate the flow around certain types of pantograph elements with reasonable accuracy and relatively lower computational cost. The turbulent Reynolds stresses in the URANS approach should be modeled through additional turbulence modeling equations. The disadvantages of URANS include the following: assuming the isotropy of normal stress turbulence and assuming that the production

of TKE to destruction equilibrium. The equations for the mean velocity components $\overline{u}_i$ and pressure ($\overline{p}$) are summarized as follows:

$$\frac{\partial \overline{u}_i}{\partial x_i} = 0, \tag{11}$$

$$\frac{\partial \overline{u}_i}{\partial t} + \overline{u}_j \frac{\partial \overline{u}_i}{\partial x_j} = \frac{1}{\rho} \frac{\partial \overline{p}}{\partial x_i} + \frac{\partial}{\partial x_j} \left(\nu \frac{\partial \overline{u}_i}{\partial x_j} \right) + \frac{1}{\rho} \frac{\partial \tau_{ij}}{\partial x_i}. \tag{12}$$

where $\tau_{ij} = \overline{u_i' u_j'}$ is the Reynolds Stress Tensor, which can be approximated in terms of the mean flow gradient together with a spatially varying turbulent viscosity based on local turbulent time/velocity and length scales [52].

It is worth mentioning that the use of Detached Eddy Simulation (DES) comprises the use of Reynolds-Averaged Navier–Stokes (RANS) and Large Eddy Simulation (LES) models to calculate the motion of small and large eddies in turbulence dominated domains. The demerit of using DES is that it might produce some problems associated with reducing the values of eddy viscosity coefficient, friction force, and Reynolds number. This reduction occurs because DES uses the LES in the calculations when the mesh becomes very dense near the surface of the wall. On the other hand, Scale-Adaptive Simulation (SAS) is very similar to URANS in its nature. SAS defines the von Karman length scale on the basis of the URANS. The use of SAS is most likely in solving the fluctuating flow field, as it does not require dividing the computational domain into URANS and LES regions [52].

The following subsections describe the simulation scenarios that were considered in the present work. For the validity of the obtained results, a comparison was made between the present results and those obtained by Siano et al. [38,39]. Then, the simulations were extended to study different models that were simulated to investigate the following parameters: (i) the effect of the pantograph speed on the flow field around the pantograph and the generated sound pressure level (SPL) at different operating conditions; (ii) the effect of modifying the panhead bars' cross-section on the generated acoustic pressure level.; (iii) the effect of the pantograph positioning on its aerodynamic performance.

4.1. Model Validation. The setup of the proposed computational model in the present article bears a close resemblance to the one proposed by Siano et al. [38]. For the validation of the present computational results, the setup of the present finite-volume model of the pantograph was adopted from the model proposed by Siano et al. [38]. Thirty-five microphone receivers were placed at a distance of 1.0 m from the symmetry plane of the pantograph to replicate the experimental acoustic field measurements, as shown in Figure 6.

Figure 6 shows the computational microphone receivers' array, which was defined on the Z- and Y-axis. For Y-axis, the array was set from a maximum value equal to 0.8 m to a minimum value equal to −0.8 m at intervals of 0.4 m. For the Z-axis, the array was set from a maximum value equal to 1.2 m to a minimum value equal to −1.2 m at intervals of
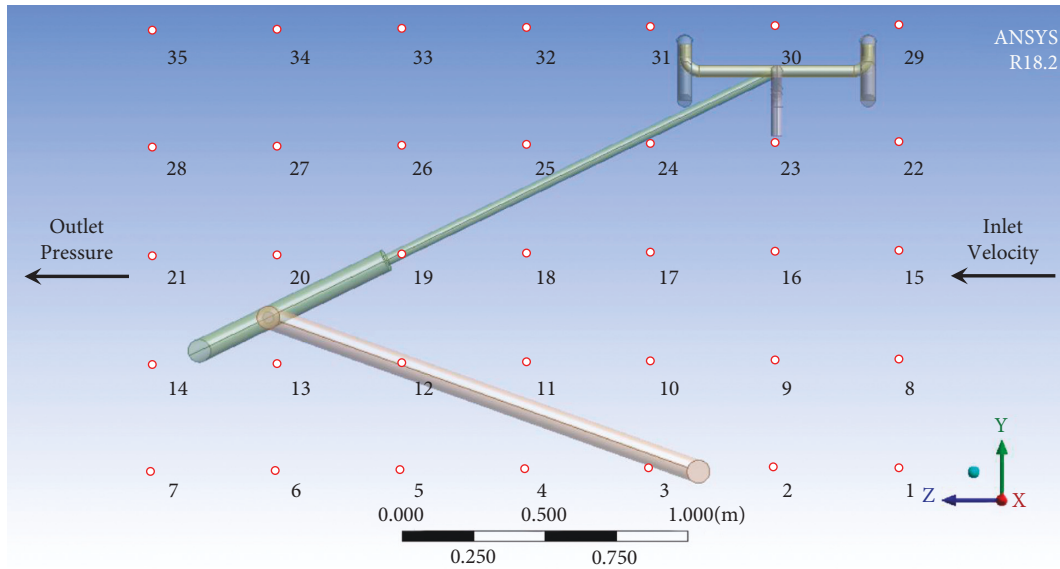
FIGURE 6: Computational receivers array positions.

0.4 m. A comparison was made between the obtained acoustic pressure from a complete pantograph simulation and those obtained from a symmetric model, as shown in Figure 7. The comparison was performed in order to check the effect of the imposed symmetric conditions on the CAA simulations of the pantograph. It was noticed that small differences were reported at the steady stage. Some additional peaks were noticed at the transient stage for the symmetric model. However, for validation purposes, the symmetric model was further used in the rest of the analysis reported in this article.

Figure 8 represents a comparison between the present results and those obtained by Siano et al. [38] for the acoustic pressure level at the pantograph. As shown in Figure 8, the signal contains a stationary and nonstationary part at a speed of 280 km/h. Measuring both transient and steady parts of the acoustic signal in one single measure is not recommended. The signal measured by the microphone receiver should be trimmed after almost 0.05 s to capture only the realistic acoustic noise of the transient part of the signal.

Small differences are noticed between the present results and those of Siano. These differences may be attributed to the differences in the exported CAD model to the simulation environment and the difference in the computational domain length. In the present model, a longer domain was considered to precisely capture the steady and transient flow fields around the pantograph.

4.2. Impact of Train Speed on the Pantograph Aeroacoustics Performance.

The simulations were extended beyond the reported measurement of the SSS87 pantograph to study the impact of train speed on the aerodynamic performance of the pantograph parts. Simulations for three models were carried out with different train speeds of 300 km/h (83.33 m/s), 320 km/h (88.89 m/s), and 340 km/h (94.44 m/s). The corresponding Mach numbers for the mentioned speeds
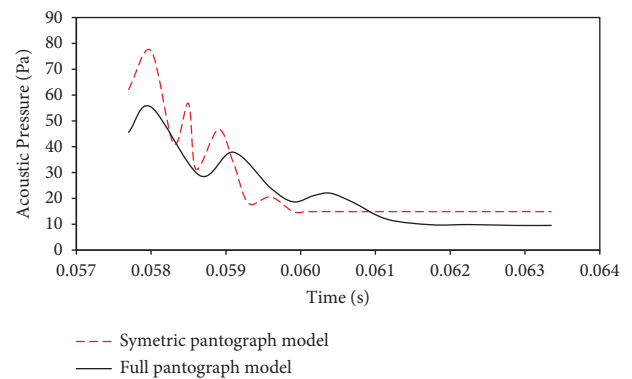

FIGURE 7: Comparison between the acoustic pressure levels calculated for a symmetric and full-scale model of SSS87 pantograph at a speed of 300 km/hr.
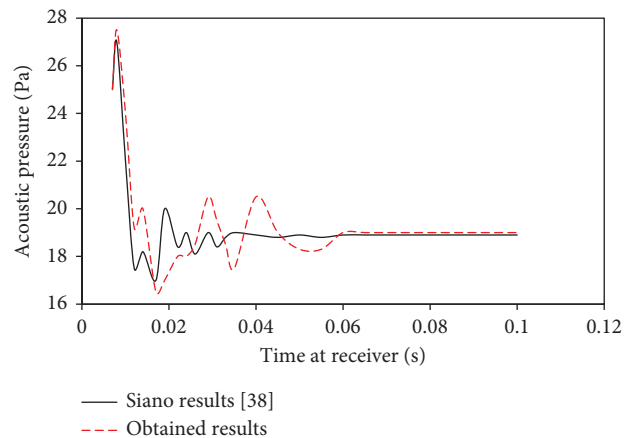

FIGURE 8: Comparison of the obtained acoustic pressure and the reported experimental results of Siano et al. [38] at a train speed of 280 km/h.

were calculated to be 0.242, 0.258, and 0.274, respectively. Then the flow in all simulation scenarios is defined as incompressible subsonic flow. A very complex flow field, including different size vortices, was noticed in the wake as the pantograph was mainly composed of rods. The instantaneous fluid flows around the pantograph at the symmetry plane can be seen in Figure 9 for a steady condition of (a) 83.33 m/s, (b) 88.89 m/s, and (c) 94.44 m/s, respectively. The turbulence model was able to accurately detect the vortex in the wake of the SSS87 pantograph. The pantograph frame is mainly composed of cylindrical bars. The dominant aerodynamic noise is then generated by the unsteady airflow around those cylindrical parts [53,54]. Strong unsteady flow separation was depicted in Figure 9 around the pantograph panhead and knee in accordance with the reported results by Lei et al. [26]. The vortex shedding is the main source of the aerodynamic noise, which usually appears at commercial operating speeds of high-speed trains. A dipole noise source is created due to the fluctuating forces created by vortices breaking up.

It is worth mentioning that the vortex shedding phenomenon occurs due to the flow separation, which arises at the values above the critical Reynolds number [54]. Due to the flow separation around the cylindrical surfaces of the pantograph, strong vortices can still be created and rapidly grow until they separate from the body. Figure 9 presents the velocity contours around the pantograph elements at different air speeds of 300 km/h, 320 km/h, and 340 km/h. As it can be seen, the regularity of the vortex structures in the flow field has changed with the inflow velocity around the pantograph. It can be seen that vortex and vorticity in the flow field also increase by increasing the velocity. However, at all simulation speeds, the vortex structure around the pantograph elements remained similar in all cases.

The vortex shedding has a significant effect on the aeroacoustics noise at different velocities [23]. It was observed that the relationship between the vortex shedding and aeroacoustics noise is proportional. Figure 10 demonstrates the growth of vortex shedding around the cylindrical parts forming the pantograph panhead in the symmetry plane. From the figure, the vortex shedding scale around the front bars of the pantograph panhead was greater than that of the rear bar.

Vortices appeared at the front cylindrical bar of the panhead and developed to collide with the vortices generated by the intermediate bar and finally hit the rear bar. This interaction between the vortices is very complex, especially at high speeds. Strong flow separation appeared, and complex flow wakes also appeared downstream due to the vortices produced from the interaction of the three cylindrical bars of the panhead.

Figure 11(a) depicts the total pressure contour for the full-scale pantograph at a speed of 300 km/hr. The figure illustrates the distribution characteristics of the whole pantograph. It can be seen that total strong pressure distribution on the front panhead bars, connecting rod, and the pantograh knee, respectively. On the other hand, Figure 11(b) illustrates the vertical structure (Q-criterion) of the pantograph. It shows the size of eddies generated by the pantograph struts. The figure presents the instantaneous

velocity magnitude colored by the vorticity. Due to the splitting of the inflow around the pantograph, foam-shaped vortices were generated, and small vortices were moved along the inflow to gradually increase and become hairpin-shaped large-scale vortices called the hairpin vortex. Different layers were detected for the generated vortex structure around the pantograph struts. The first layer originates from the front panhead bar and the second one originates from the intermediate bar and both the first and second layers are merged with the third layer from the rear bar of the pantograph panhead, as shown in Figure 11(b). The intensity of the aerodynamic noise source can be represented by the time derivative of the fluctuating pressure. Figure 12 presents the instantaneous total pressure contours around the pantograph surface. It was necessary to predict the pressure fluctuation around the pantograph components in order to perform a quantitative analysis of the sound source energy contribution rates of all components.

Figure 12 illustrates the contours of the total pressure around the pantograph in the symmetric model. As the computational setup is identical to Siano's et al. setup, it can be noted that despite the uniform and steady inlet conditions, the flow field evolves within the domain over time and this is due to the fact that turbulent flows are very unstable. In addition, given the transient model used, unfortunately, after the first transient period of the time, the flow tends to become steady, which confirms previous findings reported by Siano et al. [38, 39]. The same behavior is noticed for the total pressure, as shown in Figure 12. In combination with the analysis performed in the previous sections, the relation between the aerodynamic noise and the vortex structure was then justified and explained.

Vortex shedding at the panhead not only produces an excitation with high frequencies that influence the aeroacoustics noise but also has a strong influence on the quality of the power transmitted to the pantograph through the current collector. As a result, sparking may increase due to the fluctuation of the produced drag and lifting forces as a result of the change in the pressure level at the bars of the pantograph panhead.

The increase in the train speed leads to an increase in the wind speed around the pantograph, which leads to an increase in the acoustic pressure of the pantograph, especially at the cylindrical bars and pantograph knee. Figure 10 illustrates the variation of the acoustic pressure with time for the three different train speeds.

Figure 13 depicts the variation of the acoustic pressure with the time for train speeds of 300 km/h, 320 km/h, and 340 km/h. As can be seen in Figure 13, notable peaks of acoustic pressure were detected at a speed of 340 km/h during the transient period. These peaks are associated with the shedding and vortices breaking up around the panhead cylindrical bars. On the other hand, at speeds of 300 km/h and 320 km/h, the differences in the acoustic pressure levels are small.

4.3. Effect of Changing the Cross-Section of the Panhead Bars.
Unlike the work presented by Siano et al. [38], the present study considers the effect of the carbon layer on the top of
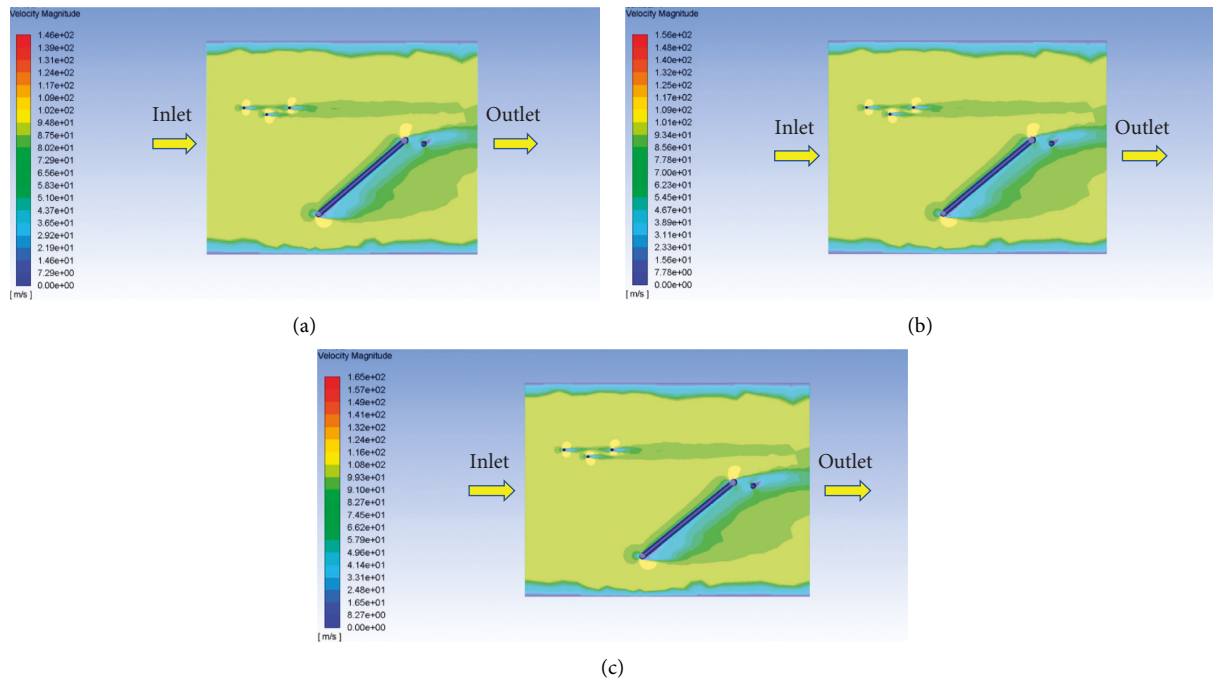
(a)

(b)

(c)

FIGURE 9: Instantaneous computational velocity contours for train speeds of (a) 300 km/h, (b) 320 km/h, and (c) 340 km/h around the pantograph in the symmetry plane.
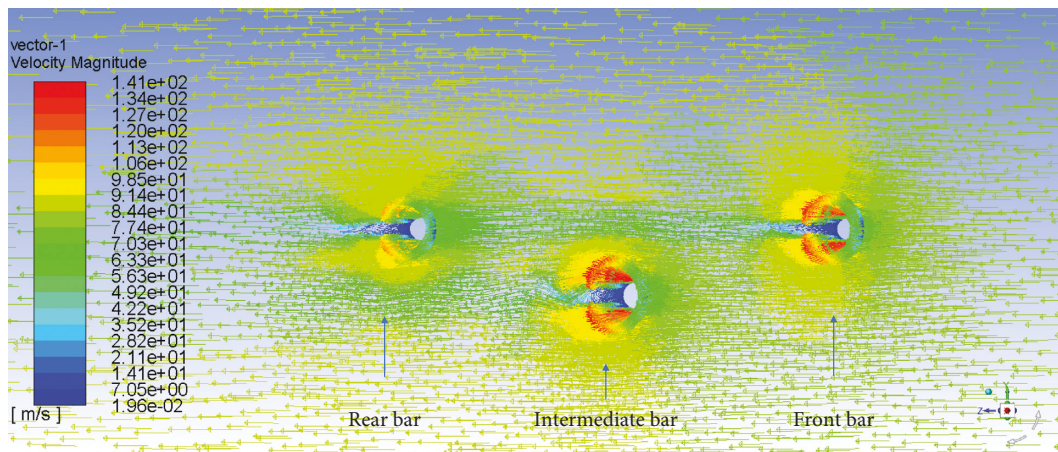

FIGURE 10: Vortex shedding around cylindrical panhead bars of the SSS87 pantograph.

the front and rear panhead cylindrical bars presenting the collector. The tested cross-sections in the present work are as follows: rounded edge in Figure 14(a); elliptic edge in Figure 14(b); diamond edge in Figure 14(c). Schematics of the modified cross-sections used to simulate the pantograph panhead are depicted in Figure 11.

Table 2 illustrates the comparison that was made for the flow fields around the three sections used. The simulations were carried out on the same pantograph model at a uniform air speed of 83.3 m/s. As shown in Figure 15, the elliptic edge cross-section shows the lowest value for the air velocity in Figure 14(a) and the maximum total pressure in Figure 14(b) around the pantograph panhead.

The figure depicts large differences between the velocity and pressure values for the different geometries of the

panhead's bar. It should be noticed that the mechanism of aerodynamic noise generation of the pantograph is affected by the turbulent kinetic energy and the pressure fluctuations and vorticities at the pantograph elements. The intensity of the aerodynamic noise is represented by the time derivative of the fluctuating pressure. From the comparison between the three geometries, it can be concluded that the fluctuating forces produced from the flow separation around the elliptic edge are low compared to those from the diamond and the rounded edge cross-sections. Thus, the aerodynamic noise associated with the vortex shedding is reduced. Moreover, the acoustic pressure level is decreased, as shown in Figure 16. Using the elliptic edge also reduces the fluctuation in the lifting forces on the pantograph leading-edge for better performance with a reduction in the probability of sparking.
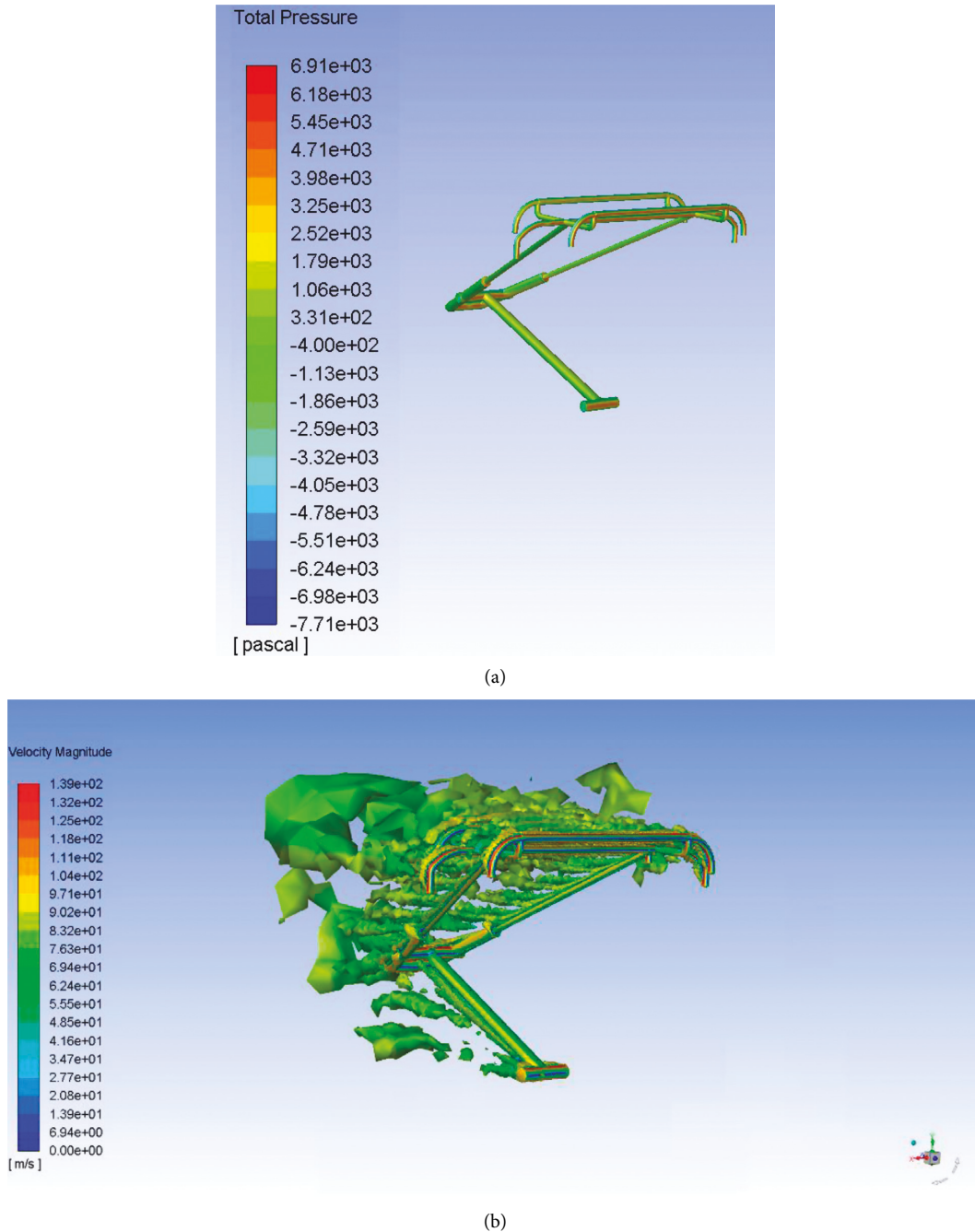
(a)

(b)

FIGURE 11: Simulation of a full pantograph model. (a) Total pressure contour; (b) instantaneous vortex structure.

4.4. Effect of the Direction of Pantograph Positioning.

The simulation was carried out on the pantograph frame for the forward and reverse modes, as shown in Figure 17, to investigate the impact of pantograph positioning on the generated aerodynamic noise.

Figure 18 depicts the total pressure characteristics on the pantograph panheads' components in forward and reverse movement directions at a train speed of 300 km/hr. The simulations were carried out using the elliptic cross-section for the front and rear parts of the pantograph panhead.

The computational fluid simulations that were carried out on the pantograph in both forward and reverse flow directions at a speed of 300 km/h provided a clear understanding of the generated aerodynamic noise from the different components of the pantograph. The highest level of noise was detected at the panhead and the coupling rode in the forward mode, whereas the highest level of noise was detected at the panhead and the knee for the reverse mode. The largest total pressure level was detected at the pantograph panhead bars, coupling rode, and knee in both modes, as shown in Figure 18.

Further aerodynamic noise analysis was performed for the pantograph panhead section as it represents the dominant source of the detected noise. A comparison was made
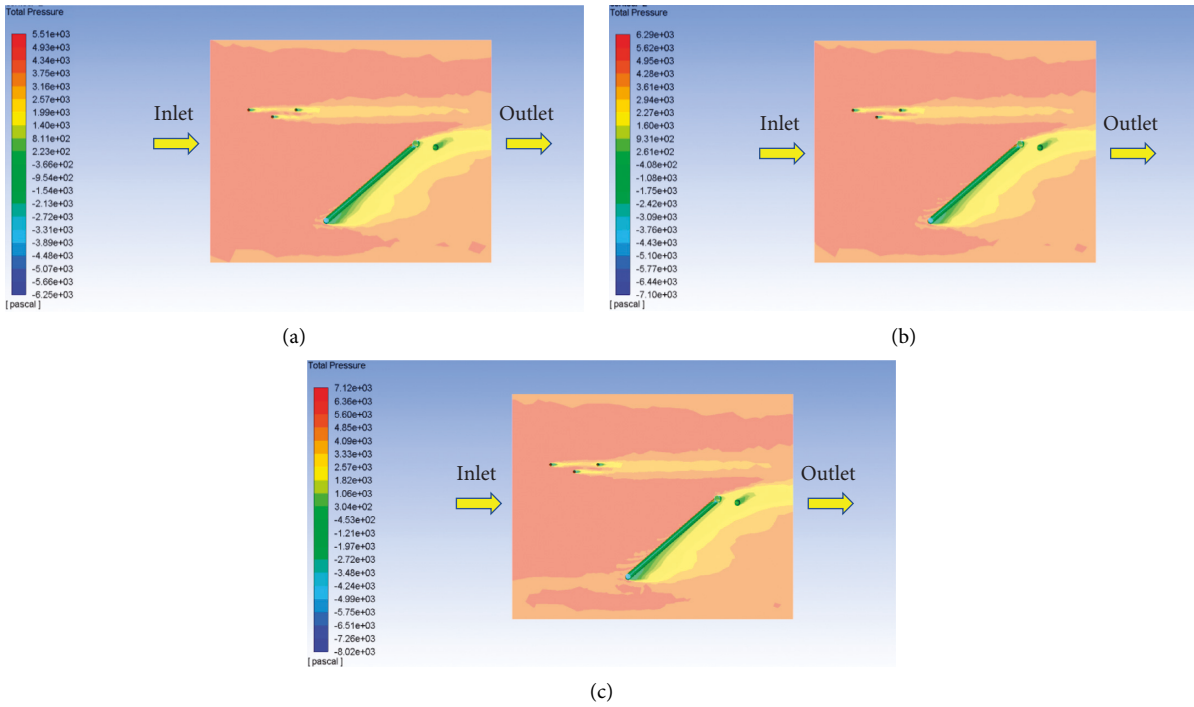
(a)

(b)

(c)

FIGURE 12: Pressure contours around the tested pantograph model in the symmetry plan at train speeds of (a) 300 km/h, (b) 320 km/h, and (c) 340 km/h.
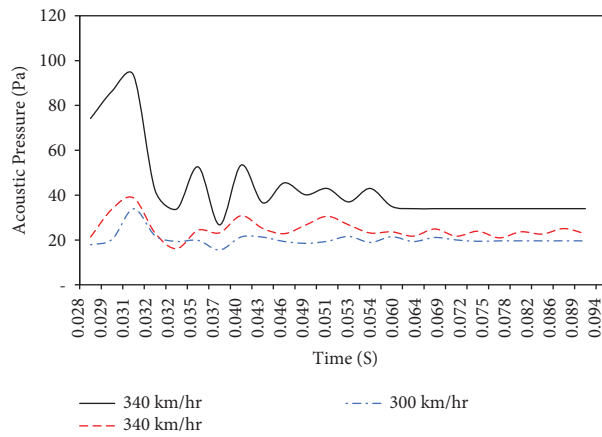

FIGURE 13: Comparison of acoustic pressure measured at the pantograph panhead for the three different train speeds.
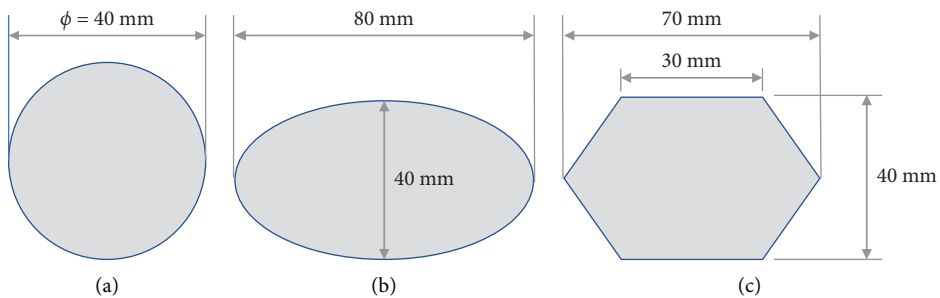

FIGURE 14: Schematic definition of the cross-sections of the panhead front and rear bars. (a) Rounded edge, (b) elliptic edge, and (c) diamond edge.

TABLE 2: Comparison of the computational results of different panhead cross-sections.

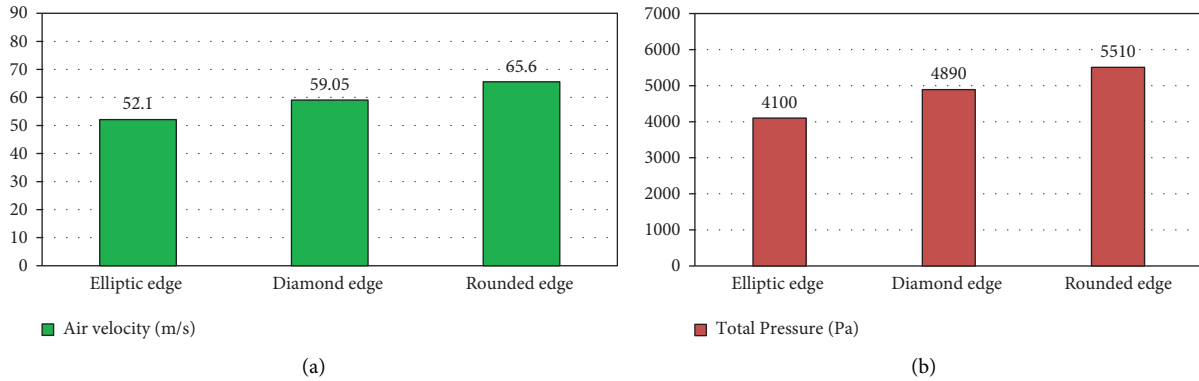| Cross-section	Velocity magnitude (m/s)	Obtained total pressure (Pa)	Calculated sound pressure (Pa)
Rounded edge	65.6	5510	74.3
Diamond edge	59.05	4890	109.22
Elliptic edge	52.1	4100	57.1

(a)

(b)

FIGURE 15: Comparison between the three different shapes of the pantograph panhead bars' cross-section.
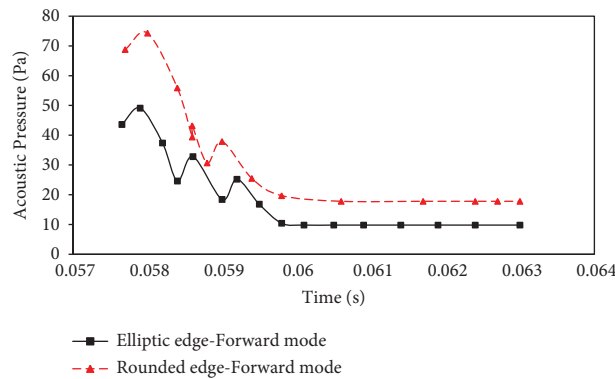

FIGURE 16: CFD results of the acoustic pressure vs. time at the receiver for the panhead with elliptic edge and rounded edge cross-section at a train speed of 250 km/h.
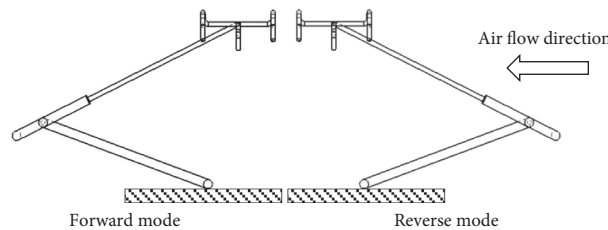

FIGURE 17: Pantograph position in forward- and reverse-motion modes as proposed in the present investigation.

for the panhead with rounded edge and elliptic edge sections at different running speeds. As the panhead with the diamond edge section exhibited the highest level of acoustic pressure, it was excluded from the comparison. The models were simulated at two uniform inlet velocities of 69.44 m/s and 83.33 m/s in both forward and reverse movement modes.

Figure 19 shows the comparison of the results of the different models at a velocity of 69.44 m/s in both forward and reverse movement modes. Notable differences were detected in the acoustic pressure during the transient period. In the steady period, the model with the elliptic edge in forward mode had the lowest acoustic pressure level, while only very small differences were detected for the

(a)   (b)
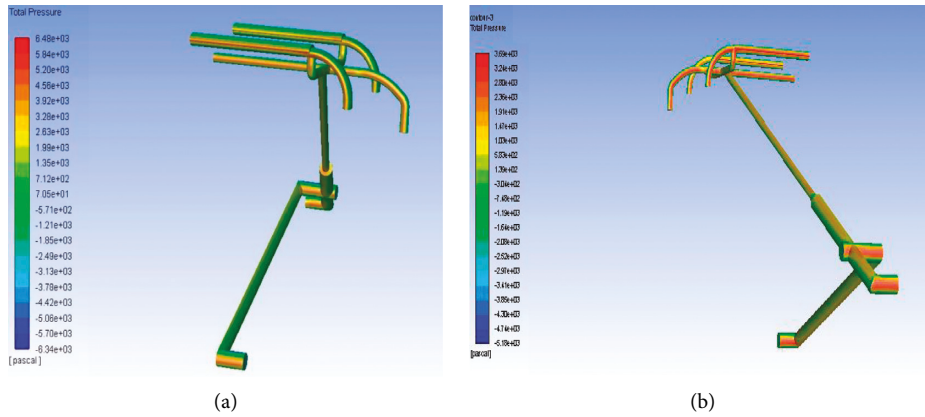
FIGURE 18: Total pressure map of the pantograph with elliptic edge cross-section at a train speed of 300 km/h: (a) forward mode and (b) reverse mode.
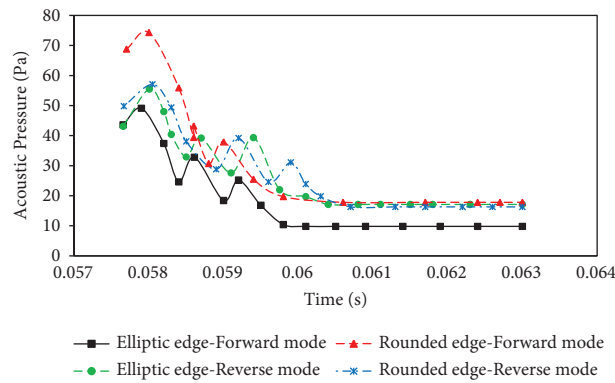

FIGURE 19: CFD results of the acoustic pressure vs. time at the receiver at an inlet velocity of 69.44 m/s (train speed of 250 km/h).
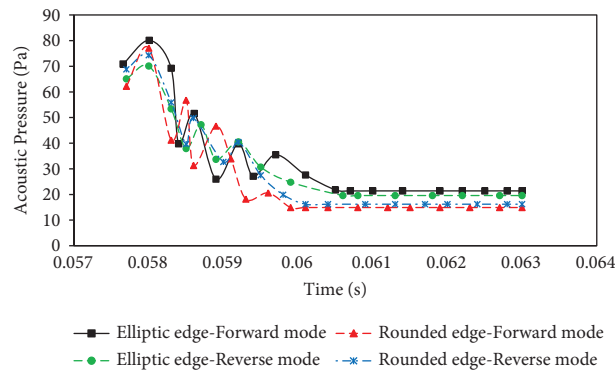

FIGURE 20: CFD results of the acoustic pressure vs. time at the receiver at an inlet velocity of 83.33 m/s (train speed of 300 km/h).

rounded edge section in both the reverse and forward modes.

At a train speed of 300 km/h, the simulation results showed that the direction of wind did not have a big impact on the generated noise at the panhead as shown in Figure 20. Small differences were detected in the acoustic pressure between the rounded edge and the elliptic edge in the forward and reverse movement modes. However, it was noticed that the model with the front and rear bars with rounded edge cross-section is still having the lowest acoustic pressure values in both the reverse and forward modes. However, the elliptic edge cross-section showed a lower potential of vortices formation, as seen in Figure 21.
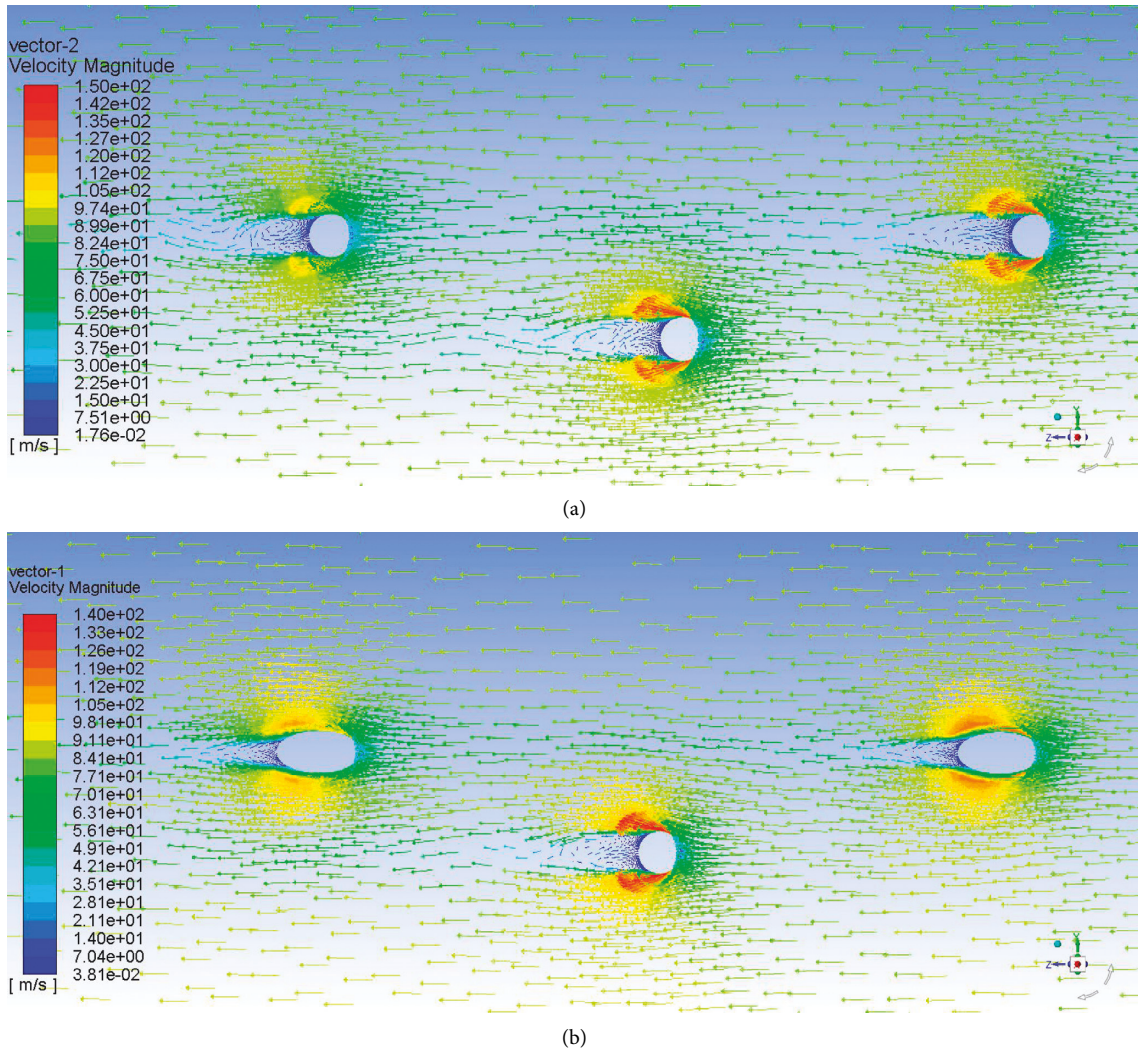
(a)

(b)

FIGURE 21: Velocity vectors for SSS87 pantograph panhead bars at a speed of 300 km/h: (a) Rounded edge cross-section; (b) elliptic edge cross-section.

From Figure 21, the elliptic edge section offered lower fluctuations in the aerodynamic forces affecting the panhead compared to the rounded edge cross-section. For this reason, it could be a potential replacement for the rounded edge to reduce the spark formations that affect the quality of the transmitted power to the high-speed trains.

5. Conclusions

One of the major sources of noise for high-speed trains is the pantograph aerodynamic noise. At high operating speeds above 300 km/h, the aerodynamic noise grows to be comparable to the rolling contact noise. To reduce pantograph noise, it is necessary to understand the noise creation mechanism for a pantograph. However, it is difficult to estimate this mechanism due to the complexity of the pantograph components. By using computational modeling, it is possible to detect the portion of the pantograph that generates the highest level of noise. For these reasons, advanced aerodynamic noise prediction using computational simulations is accurate, reliable, and efficient.

The present article uses a computational model to assess the aerodynamic noise from a high-speed pantograph. The obtained results from the computational simulations were verified against the computational and experimental measurements in the literature for the same pantograph model. The simulations were carried out on the pantograph using different train running speeds. It was found that the vortex shedding at the pantograph's panhead was the dominant source of the noise. Large flow separation was detected at the cylindrical bars forming the panhead, which leads to the acoustic pressure fluctuations at the panhead.

Different designs for the pantograph's panhead front and rear bars were suggested to reduce the aerodynamic noise generated at the panhead part. It was found that the found pressure level increased by almost 47% when using a diamond-shaped edge section as a replacement for the cylindrical cross-section of the front and rear bars of the panhead. Based on the obtained computational results, it was found

that the use of an elliptic edge cross-section bars can be a potential modification in the collector shape that can reduce the aerodynamic noise at the panhead for speeds up to 250 km/h. A reduction of 23.1% in the sound pressure levels was detected in the case of using the elliptic cross-section. For higher velocities up to 340 km/h, the elliptic edge sections can also be used as a potential solution for reducing the possibility of sparking. In both forward and reverse movement mode, it was noticed that the highest level of aerodynamic noise was detected at the pantographs' panhead, knee, and coupling rode. However, at a speed of 300 km/h, small differences between the values of the acoustic pressure were noticed only during the transient period. Further investigations are still needed to optimize the dimensions of the carbon strips with the positioning and geometry modifications of the cylindrical bars forming the panhead.

Data Availability

The data used to support this study are included within the article.

Conflicts of Interest

The authors declare that they have no conflicts of interest.

References

[1] B. Schulte-Werning, D. Thompson, P.-E. Gautier et al., *Noise and vibration mitigation for rail transportation systems: proceedings of the 9th International Workshop on Railway Noise*, Springer Science & Business Media, Berlin, Germany, 2008.

[2] D. Thompson, *Railway Noise and Vibration: Mechanisms, Modelling and Means of Control*, Elsevier, Amsterdam, Netherlands, 2008.

[3] X. Zhang, "Empirical modeling of railway aerodynamic noise using one microphone pass-by recording," in *Noise and Vibration Mitigation for Rail Transportation Systems*Springer, Berlin, Germany, 2015.

[4] B. He, X. Xiao, X. Zhou, J. Han, and X. Jin, "Characteristics of sound insulation and insertion loss of different deloading sound barriers for high-speed railways," in *Noise and Vibration Mitigation for Rail Transportation Systems*, pp. 345–352, Springer, Berlin, Germany, 2015.

[5] F. Poisson, "Railway noise generated by high-speed trains," in *Noise and Vibration Mitigation for Rail Transportation Systems*, pp. 457–480, Springer, Berlin, Germany, 2015.

[6] J. Galuba and C. Spehr, "Concept for measuring aeroacoustic noise transmission in trains derived from experience gained in aircraft testing," in *Noise and Vibration Mitigation for Rail Transportation Systems*, pp. 165–172, Springer, Berlin, Germany, 2015.

[7] M. Mohebbi and A. M. Safaee, "The optimum model determination of porous barriers in high-speed tracks," *Proceedings of the Institution of Mechanical Engineers - Part F: Journal of Rail and Rapid Transit*, vol. 236, no. 1, pp. 15–25, 2022.

[8] M. Mohebbi and M. A. Rezvani, "2D and 3D numerical and experimental analyses of the aerodynamic effects of air fences on a high-speed train," *Wind and Structures*, vol. 32, no. 6, pp. 539–550, 2021.

[9] M. Mohebbi and M. A. Rezvani, "The impact of air fences geometry on air flow around an ICE3 high speed train on a double line railway track with exposure to crosswinds," *Journal of Applied Fluid Mechanics*, vol. 11, no. 3, pp. 743–754, 2018.

[10] M. A. Rezvani and M. Mohebbi, "Numerical calculations of aerodynamic performance for ATM train at crosswind conditions," *Wind and Structures*, vol. 18, no. 5, pp. 529–548, 2014.

[11] M. Mohebbi and M. A. Rezvani, "Two-dimensional analysis of the influence of windbreaks on airflow over a high-speed train under crosswind using lattice Boltzmann method," *Proceedings of the Institution of Mechanical Engineers—Part F: Journal of Rail and Rapid Transit*, vol. 232, no. 3, pp. 863–872, 2018.

[12] M. Mohebbi and M. A. Rezvani, "Multi objective optimization of aerodynamic design of high speed railway windbreaks using Lattice Boltzmann Method and wind tunnel test results," *International Journal of Reality Therapy*, vol. 6, no. 3, pp. 183–201, 2018.

[13] M. Mohebbi and M. A. Rezvani, "Numerical analysis of aerodynamic performance of regional passenger train under crosswind conditions," *International Journal of Vehicle Structures & Systems*, vol. 5, no. 2, p. 68, 2013.

[14] T. Kurita, M. Hara, H. Yamada et al., "Reduction of pantograph noise of high-speed trains," *Journal of Mechanical systems for Transportation and Logistics*, vol. 3, no. 1, pp. 63–74, 2010.

[15] T. Mitsumoji, T. Sueki, N. Yamazaki et al., "Aerodynamic noise reduction of a pantograph panhead by applying a flow control method," in *Noise and Vibration Mitigation for Rail Transportation Systems,* Springer, Berlin, Germany, 2015.

[16] C. Noger, J. Patrat, J. Peube, and J. Peube, "Aeroacoustical study of the TGV pantograph recess," *Journal of Sound and Vibration*, vol. 231, no. 3, pp. 563–575, 2000.

[17] K. Nagakura, "Localization of aerodynamic noise sources of Shinkansen trains," *Journal of Sound and Vibration*, vol. 293, no. 3-5, pp. 547–556, 2006.

[18] Y. Lee, J. Rho, M. Kwak, J. Lee, K. Kim, and D. Lee, "Aerodynamic characteristics of high speed train pantograph with the optimized panhead shape," in *Proceedings of the International Conference on FLUID MECHANICS and Aerodynamics 2009*, Moscow, Russia, 2009.

[19] T. Lalgen, "Wind tunnel noise measurements on full-scale pantograph models," *Journal of the Acoustical Society of America*, vol. 105, no. 2, 1999.

[20] C. Guo-Hua, "The experimental technique of pantograph of super express train in low speed wind tunnel," *Journal of Railway Engineering Society*, vol. 4, pp. 67–70, 2006.

[21] A. Lauterbach, K. Ehrenfried, S. Loose, and C. Wagner, "Microphone array wind tunnel measurements of Reynolds number effects in high-speed train aeroacoustics," *International Journal of Aeroacoustics*, vol. 11, no. 3-4, pp. 411–446, 2012.

[22] K. Manabe and T. Okubo, "The aerodynamic sound from pantograph and the reducing method (1)—wind tunnel tests on the existing pantograph (in Japanese)," *Railway Technical Research Report*, vol. 1237, pp. 655–671, 1983.

[23] H.-M. Noh, "Wind tunnel test analysis to determine pantograph noise contribution on a high-speed train," *Advances in Mechanical Engineering*, vol. 11, no. 10, Article ID 1687814019884778, 2019.

[24] M. Ikeda and T. Mitsumoji, "Evaluation method of low-frequency aeroacoustic noise source structure generated by

Shinkansen pantograph," *Quarterly Report of RTRI*, vol. 49, no. 3, pp. 184–190, 2008.

[25] M. Ikeda and T. Mitsumoji, "Numerical estimation of aerodynamic interference between panhead and articulated frame," *Quarterly Report of RTRI*, vol. 50, no. 4, pp. 227–232, 2009.

[26] S. Lei, Z. Chengchun, W. Jing, and R. Luquan, "Numerical analysis of aerodynamic noise of a high-speed pantograph," in *Proceedings of the 2013 Fourth International Conference on Digital Manufacturing & Automation*, IEEE, Shinan, China, 2013.

[27] E. L. Iglesias, D. Thompson, and M. Smith, "Component-based model to predict aerodynamic noise from high-speed train pantographs," *Journal of Sound and Vibration*, vol. 394, pp. 280–305, 2017.

[28] W. Behr, T. Lolgen, W. Baldauf et al., "Low noise pantograph ASP-recent developments," in *Proceedings of the 29th International Congress on Noise Control Engineering*, Nice, France, 2000.

[29] W. Baldauf, R. Blaschko, W. Behr, C. Heine, and M. Kolbe, "Development of an actively controlled, acoustically optimised single arm pantograph," in *Proceedings of the World Congress of Railway Research WCRR 2001*, Cologne, Germany, 2001.

[30] M. Ikeda, T. Mitsumoji, T. Sueki, and T. Takaishi, "Aerodynamic noise reduction in pantographs by shape-smoothing of the panhead and its support and by use of porous material in surface coverings," *Quarterly Report of RTRI*, vol. 51, no. 4, pp. 220–226, 2010.

[31] T. Xiao-Ming, Y. Zhi-Gang, T. Xi-ming, W. Xiao-long, and Z. Jie, "Vortex structures and aeroacoustic performance of the flow field of the pantograph," *Journal of Sound and Vibration*, vol. 432, pp. 17–32, 2018.

[32] M. Suzuki, M. Ikeda, and K. Yoshida, "Study on numerical optimization of cross-sectional panhead shape for high-speed train," *Journal of mechanical systems for transportation and logistics*, vol. 1, no. 1, pp. 100–110, 2008.

[33] T. Takaishi and M. Ikeda, "Experimental method for wind tunnel tests to simulate turbulent flow on the roof of high-speed trains," *Quarterly Report of RTRI*, vol. 53, no. 3, pp. 167–172, 2012.

[34] S. Bruni, J. Ambrosio, A. Carnicero et al., "The results of the pantograph–catenary interaction benchmark," *Vehicle System Dynamics*, vol. 53, no. 3, pp. 412–435, 2015.

[35] J. Pombo, J. Ambrósio, M. Pereira, F. Rauter, A. Collina, and A. Facchinetti, "Influence of the aerodynamic forces on the pantograph–catenary system for high-speed trains," *Vehicle System Dynamics*, vol. 47, no. 11, pp. 1327–1347, 2009.

[36] J. Ambrósio, J. Pombo, and M. Pereira, "Optimization of high-speed railway pantographs for improving pantograph-catenary contact," *Theoretical and Applied Mechanics Letters*, vol. 3, no. 1, Article ID 013006, 2013.

[37] B. Andersson, *Manual in case of breakdown of pantographs Instructions for working grounding of vehicles and disassembly of pantographs*, Swedish Transport Administration, Borlänge, Sweden, 2019.

[38] D. Siano, M. Viscardi, F. Donisi, and P. Napolitano, "Numerical modeling and experimental evaluation of an high-speed train pantograph aerodynamic noise," *Computers and Mathematics in Automation and Materials Science*, vol. 12, no. 1, pp. 86–92, 2011.

[39] M. Viscardi, D. Siano, P. Napolitano, and F. Donisi, "An analytical model for the aerodynamic noise prediction of an high-speed train pantograph," *Applied Informatics and Communications*, pp. 271–280, 2014.

[40] ANSYS, *Fluent 18.2 User's Manual*ANSYS Ltd, Canonsburg, PA, USA, 2018.

[41] R. Ewert and W. Schröder, "Acoustic perturbation equations based on flow decomposition via source filtering," *Journal of Computational Physics*, vol. 188, no. 2, pp. 365–398, 2003.

[42] R. Ewert and W. Schröder, "On the simulation of trailing edge noise with a hybrid LES/APE method," *Journal of Sound and Vibration*, vol. 270, no. 3, pp. 509–524, 2004.

[43] J. F. Williams and D. L. Hawkings, "Sound generation by turbulence and surfaces in arbitrary motion," *Philosophical Transactions of the Royal Society of London - Series A: Mathematical and Physical Sciences*, vol. 264, pp. 321–342, 1969.

[44] H.-H. Yu, J.-C. Li, and H.-Q. Zhang, "On aerodynamic noises radiated by the pantograph system of high-speed trains," *Acta Mechanica Sinica*, vol. 29, no. 3, pp. 399–410, 2013.

[45] Y. Zhang, J. Zhang, T. Li, and L. Zhang, "Investigation of the aeroacoustic behavior and aerodynamic noise of a high-speed train pantograph," *Science China Technological Sciences*, vol. 60, no. 4, pp. 561–575, 2017.

[46] Y. Yao, Z. Sun, G. Yang, W. Liu, and P. Prapamonthon, "Analysis of aerodynamic noise characteristics of high-speed train pantograph with different installation bases," *Applied Sciences*, vol. 9, no. 11, p. 2332, 2019.

[47] D. Lockard, "A comparison of Ffowcs Williams-Hawkings solvers for airframe noise applications," in *Proccedings of the 8th AIAA/CEAS Aeroacoustics Conference & Exhibit*, Breckenridge, CO, USA, 2002.

[48] T. Li, D. Qin, W. Zhang, and J. Zhang, "Study on the aerodynamic noise characteristics of high-speed pantographs with different strip spacings," *Journal of Wind Engineering and Industrial Aerodynamics*, vol. 202, Article ID 104191, 2020.

[49] D. G. Crighton, A. P. Dowling, J. Ffowcs-Williams, M. Heckl, F. Leppington, and J. F. Bartram, *Modern Methods in Analytical Acoustics Lecture Notes*Acoustical Society of America, Melville, NY, USA, 1992.

[50] D. P. Lockard, "An efficient, two-dimensional implementation of the Ffowcs Williams and Hawkings equation," *Journal of Sound and Vibration*, vol. 229, no. 4, pp. 897–911, 2000.

[51] S. Chen and G. D. Doolen, "Lattice Boltzmann method for fluid flows," *Annual Review of Fluid Mechanics*, vol. 30, no. 1, pp. 329–364, 1998.

[52] S. Wang, J. R. Bell, D. Burton, A. H. Herbst, J. Sheridan, and M. C. Thompson, "The performance of different turbulence models (URANS, SAS and DES) for predicting high-speed train slipstream," *Journal of Wind Engineering and Industrial Aerodynamics*, vol. 165, pp. 46–57, 2017.

[53] R. Blevins, "The effect of sound on vortex shedding from cylinders," *Journal of Fluid Mechanics*, vol. 161, pp. 217–237, 1985.

[54] C. H. Williamson, "Oblique and parallel modes of vortex shedding in the wake of a circular cylinder at low Reynolds numbers," *Journal of Fluid Mechanics*, vol. 206, pp. 579–627, 1989.